scientific reports

Check for updates

OPEN

Mechanical characterization and impact damage assessment of Al/SiC functionally graded coating under elevated temperatures

D. Muniraj, S. Vignesh & V. M. Sreehari✉

Functionally graded materials are a class of composite materials that finds widespread use in aerospace, defense and automobile applications due to their tailored material properties for the specific need. In the present research, impact dynamics and the damage behavior of functionally graded plasma spray coating (FGPS) on an aluminium 6061-T6 substrate under high velocity impact at various temperatures were studied. The FGPS coating consists of four layers having various proportions of Al and SiC (50/50, 40/60, 30/70 and 20/80 weight percentages) and the coating thickness was measured to be 232.8 µm. Experiments were carried out at 260 J of impact energy on the FGPS samples at various temperatures using a single-stage gas gun along with the thermal setup. A finite element model was developed with the Johnson-Cook damage model and piecewise linear plasticity material model, along with suitable contact algorithms. Impact simulations at various temperatures reveal that the stiffness reduction at higher temperatures results in decreased peak contact force, decreased rebound velocity and increased central deflection. The molten splats observed through the micro-morphological study have spread several micrometers, which indicates excellent bonding between the particles and the porosity content was found to be 1.35%. The research findings on the impact dynamics and damage behavior of FGPS can significantly improve material design for a wide range of applications.

Keywords Functionally graded material, Plasma spray coating, High velocity impact, Elevated temperature

List of symbols

V_c	Volume fraction of ceramic
V_m	Volume fraction of metal
ν_c	Poisson's ratio of ceramic
ν_m	Poisson's ratio of metal
ρ_c	Density of ceramic
ρ_m	Density of metal
E	Young's modulus
E_c	Young's modulus of ceramic
E_m	Young's modulus of metal
q	Stress-strain transfer rate
σ_Y	Yield stress of the composite
σ_0	Yield stress of the metal
n_0	Hardening exponent of metal
A	Initial yield stress of the material
B	Strain hardening constant
C	Strengthening coefficient of strain rate
T_{Melt}	Melting temperature
T_{Room}	Room temperature
D	Damage parameter of an element
p	Strain hardening coefficient
m	Thermal softening coefficient

School of Mechanical Engineering, SASTRA Deemed University, Thanjavur 613401, Tamilnadu, India. ✉email: sreehari_vm@mech.sastra.edu

Functionally graded materials (FGMs) are a class of composite material with a unique graded structure, where the mixture and/or arrangement of the material varies from one end to the other, enabling the material to exhibit distinctive properties. These properties can be optimized for specific applications, including mechanical, thermal, or electrical, making FGMs an attractive choice for aerospace, defense and automotive applications[1,2]. FGMs can be made by combining different materials, such as metals and ceramics, in a way that allows for a smooth transition between them to reduce the stress concentration that occurs at the coherent zone between two different materials in typical composites. FGMs experience numerous types of thermo-mechanical loads combinations such, as tensile, flexural, impact, oxidation and wear along with the thermal load. The metal-ceramic FGM having stable thermo-mechanical properties is the right choice of material to endure such loading conditions. The ceramic content can provide high stiffness and wear resistance, while the metal content can provide ductility and toughness.

FGMs made using a variety of processes, including powder metallurgy, physical and chemical vapor deposition, plasma spray and infiltration[1,3]. Dual-beam pulsed laser deposition was used by Deng et al.[4] to fabricate functionally-graded yttria-stabilized zirconia (YSZ) coatings and examined the thermal conductivity and bonding strength. Lin et al.[5] produced bulk FGM through the powder metallurgy process by cold and hot compaction and studied the microstructure and hardness. Plasma spray is a coating technique that is used to coat the melted powder particles on the substrate[6–9]. Zhang et al.[10] produced the SiC fibre-reinforced SiC ceramic matrix composite substrate and coated it with Si and Yb_2SiO_5 using an atmospheric plasma spray technique. Seifert et al.[11] developed the mullite powder coating on the aluminium substrate through various spray parameters for the space vehicle application. Khor and Gu[12] manufactured the five-layer functionally graded thermal barrier coatings (yttria-stabilized ZrO_2 and NiCoCrAlY) and investigated their thermal characteristics. Goudarzi et al.[13] created four distinct thick thermal barrier coatings over stainless steel 420 base and evaluated their microstructural analysis, bonding strength to the substrate, micro-hardness and thermal endurance.

Thirumalaikumarasamy et al.[14] investigated the influence of powder feed rates, stand-off distances, and power on the alumina coating over AZ31B magnesium alloy by atmospheric plasma and found that the micro-hardness was significantly affected by input power. Wu et al.[15] used a ferrous-based coating to improve the hardness of a stainless steel substrate, and the coating's micro-hardness value increased four times that of the substrate. Yongzhong and Donghui[16] enhanced the microhardness of S275JR structural steel through an AlCrNi coating that was twice as hard as the substrate. Habib et al.[17] utilized flame spraying oxygen-fuel and high-velocity oxygen fuel (HVOF) thermal spraying methods to developed the Ni-based alloy coating on an AISI 304 substrate. They discovered that the micro-hardness values of the oxygen-fuel technique were 9% higher than those of the HVOF technique. Patel et al.[18] manufactured the thermally sprayed polyether ether ketone on ANSI 304 stainless steel substrates with a variable roughness parameter and found that the surfaces with appropriate topography provide higher mechanical interlocking than the chemistry of the substrate. An air plasma spray technique was used by Patibanda et al.[19] to coat the YSZ on the stainless steel substrate and found that the average roughness was 10 μm using a 3D optical micrograph. The abrupt temperature change results in crack initiation, property degradation, and delamination of the coating because of the difference in thermal expansion[20]. Loghman-Estarki et al.[21] used an air-plasma sprayed process to create the Ni-based super alloy coating and performed a thermal shock test to confirm that the 7 weight% (wt%) YSZ had a longer life span of 246 cycles. Huang et al.[22] used the plasma spray approach to apply a $LaPO_4$/8YSZ coating to a nickel substrate and tested its thermal shock resistance.

Micrometeoroids, space debris, hail ice, bullets, and bird strikes cause high-velocity impact loads on air and space vehicles. As a result, research is still required to understand material's damage behavior. Sahu et al.[23] utilized the Johnson-Cook material model to assess the material's dynamic response and compared the computational and experimental data, revealing an accurate stress-strain curve. Chocron et al.[24] investigated the Johnson-Cook material model in ballistic applications and discovered that both experimental and computational ballistic tests on various thicknesses of aluminium plate exhibit the same failure pattern. By simulating an impact event using the Johnson-Holmquist material model, Krishnan et al.[25] found that the outcome of the numerical model of ceramic composite armor matches well with the experimental data. Sinha et al.[26] examined the high-velocity missile impact and its detonation on an aircraft engine nozzle and found that the blast pressure wave creates more damage after the structural damage created by the missile. Rhymer and Kim[27] simulated an ice ball projectile impact on composite to scrutinize the impact physics of carbon/epoxy composite panels. On bonded joints, Li et al.[28] performed an impact and tensile test at various temperatures and impact energies. According to Liu et al.'s[29] investigation into the functionally graded foam's impact response and energy absorption in a temperature gradient environment, the gradient enlarges the deformed regions. Lee and Kim[30] proposed the mathematical model for functionally graded material and analyzed the thermal load and aerodynamic heating during hypersonic flow.

Stable thermomechanical properties at a low weight is the main criteria for the aerospace material selection. Most of the literature on FGM has focused on the wear, oxidation and thermal shock resistance; additional research on the advanced composites under impact loads at elevated temperatures is still required. Thus, the present research work fills the research gap by investigating the structural response of FGPS plates under high-velocity impact at various temperatures. Al/SiC FGPS coating was performed on the aluminium 6061-T6 substrate using the plasma spray technique and mechanical characterization was performed. A single stage gas gun was employed to conduct experiments on the FGPS plate under 260 J impact energy at different temperatures. LS-DYNA software was used to conduct computational simulations to study the impact dynamics.

Experimental methodology

Fabrication of FGPS plate

An aluminium 6061-T6 plate of 5 mm thick and 300 mm × 300 mm in size is used as the base plate for the functionally graded plasma spray coating. The functionally graded coating consists of metal to ceramic-rich variations in which aluminium 6061 and silicon carbide powders are used as metal and ceramic constituents, respectively. The required proportions of metal and ceramic constituents are weighed and ball milled for thorough mixing. Plasma is created by passing a mixture of hydrogen and argon gas through an electric arc, which rapidly heats and expands the gas. The pre-mixed powders are fed into the plasma, which melts and is propelled towards the substrate. In the end, coating is carried out as Fig. 1 illustrates. An injector of 5 mm diameter is used from a spraying distance of 152 mm at 90 degree injector angle. A bond coat of nickel chromium is given initially, before the FG coating. The metal-ceramic FG coating consists of four layers, starting with Al (50%) by weight and SiC (50%) as the bottom layer, subsequently Al (40%) and SiC (60%) as the third layer, Al (30%) and SiC (70%) as second layer and the top most layer, Al (20%) and SiC (80%) as ceramic rich.

High velocity impact test

The single-stage gas gun test system, shown in Fig. 2(a), was used to facilitate the high velocity impact experiments. The gas gun has a reciprocating compressor that compresses and stores the air in a high-pressure reservoir at the required impact velocity. The manufactured FGPS plate is shown in Fig. 2b. A spherical stainless steel projectile (Fig. 2c) with 67 g mass and 25.4 mm diameter is used in the present study. The projectile is placed next to the solenoid valve, which allows the projectile to propel to the required velocity when the valve releases high pressure air suddenly. All the tests were conducted at 5 bar pressure at an impact velocity of 88 m/s. At the end of the launch tube, two photoelectric sensors were employed for measuring the projectile's velocity. To execute high-velocity impact tests at various temperatures, the manufactured FGPS plate was first placed in the furnace's test fixture (Fig. 2d) and heated to the desired temperature. Then the same temperature was maintained for 20 min to get the uniform temperature distribution and eventually the impact tests were carried out.

Material characterization and basic mechanical tests

A scanning electron microscope was employed to investigate the FGPS coating's microstructure. To measure the coating thickness of an FGPS sample, two samples of 10 mm × 10 mm were cut with the aid of wire-cut EDM and joined at the coating surfaces with epoxy. The glued samples were viewed from the top in such a way to measure the thickness along the cross section. Measurements were made at nine different places in order to estimate the average thickness of the FG coating. Tensile tests were conducted based on the ASTM E8 standard in a Universal Testing Machine setup to estimate the yield and ultimate strength and understand the fracture behavior of the substrate and coating. A flexural test (3-point bending test) was done in accordance with the ASTM D790 standard to further understand the coating's flexural delamination. Figure 3a depicts the three-point bending test in which a vertical load is given to the non-coated side of the FGPS beam between the two roller supports

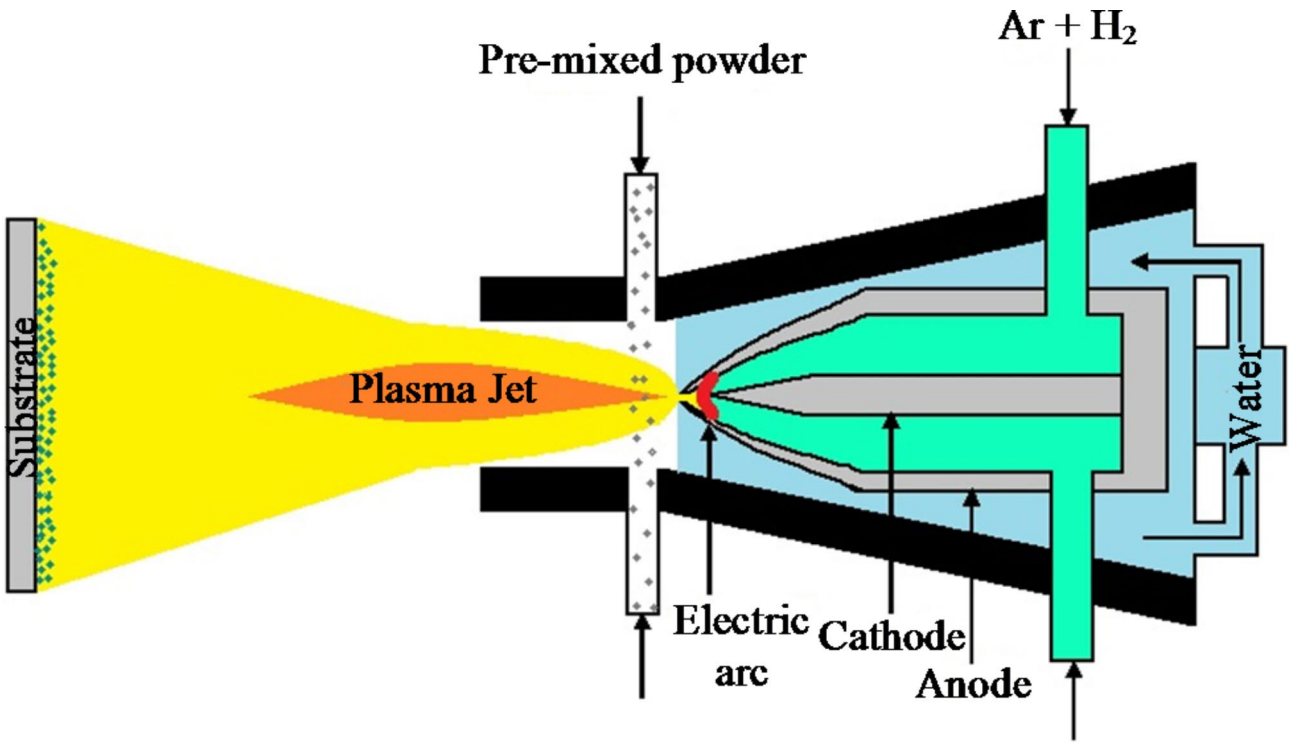

Fig. 1. Schematic representation of plasma spray technique.

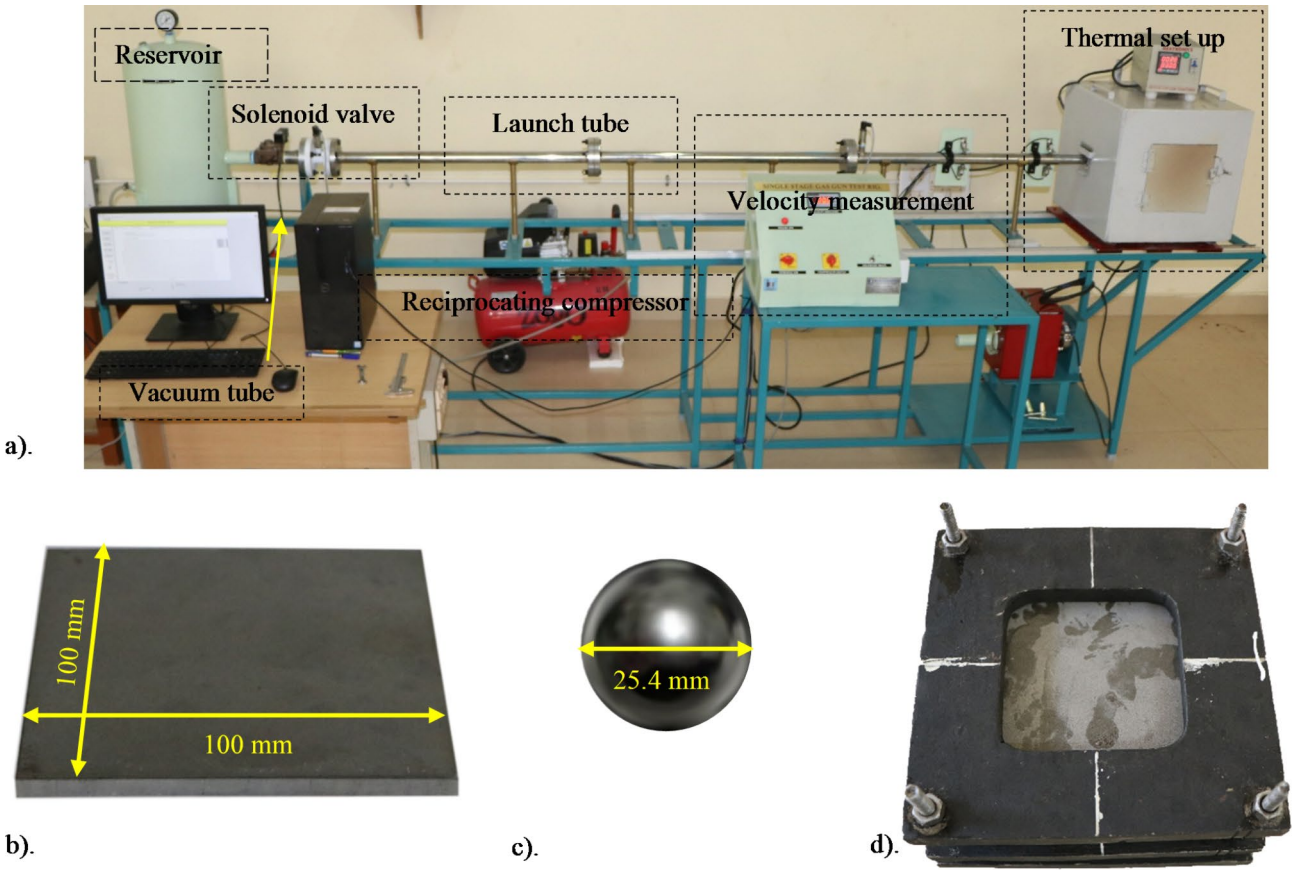

Fig. 2. High velocity impact equipment with thermal test setup: (**a**) Single stage gas gun. (**b**) FGPS plate. (**c**) Steel Projectile. (**d**) Test fixture.

R_1 and R_2. The surface hardness of the FGPS coating was measured with a Vickers micro-hardness instrument. The FGPS specimen was indented with a diamond indenter, and the micro-hardness was then measured using the diagonals of impression in accordance with the applied force. A load of 9.807 N (Fig. 3b) was applied for a retention time of 10 s at 5 different locations and determined the micro-hardness. Surface roughness is a crucial factor that determines the friction factor and wear parameters, which depend on the coating smoothness or roughness when they interact with each other. With a 0.8 mm cutoff length and a 4 mm sampling length, the roughness test was carried out using a surface roughness tester. The measurements were taken at three different locations of FGPS surface and non-coated base plate. The thermal shock test (Fig. 3c) involved placing a 10 mm × 10 mm FGPS specimen in a muffle furnace for 5 min at an operating temperature of 705 K ± 20 K and then quenching it in water for 5 min. This cycle was repeated until delamination occurred in the coating. The number of thermal cycles needed to cause the coating to delaminate from the substrate was counted in order to understand thermal behavior.

Theoretical model

The FGPS plate has four layers of coating with various proportions of metal and ceramic components. The theoretical model is used to ascertain the properties of the layer wise coating through power law, rule of mixture and the Tamura-Tomota-Ozawa model (TTO)[31]. The volumetric fraction (V) of the ceramic (c) and metal (m) for each layer is given by Eq. (1)

$$V_c + V_m = 1 \tag{1}$$

The metallic volume fraction's functional gradation in the thickness direction (z) is constructed using the power law distribution, as stated in Eq. (2), where n, the compositional gradient exponent used to control the layer wise coating composition that can be varied either linearly ($n=1$) or non-linearly and t, the coating thickness.

$$V_m\ (z) = \left(1 - \frac{z}{t}\right)^n \tag{2}$$

Equations (3) and (4) give the Poisson's ratio and the composite's density.

$$v_z = V_c v_c + V_m v_m \tag{3}$$

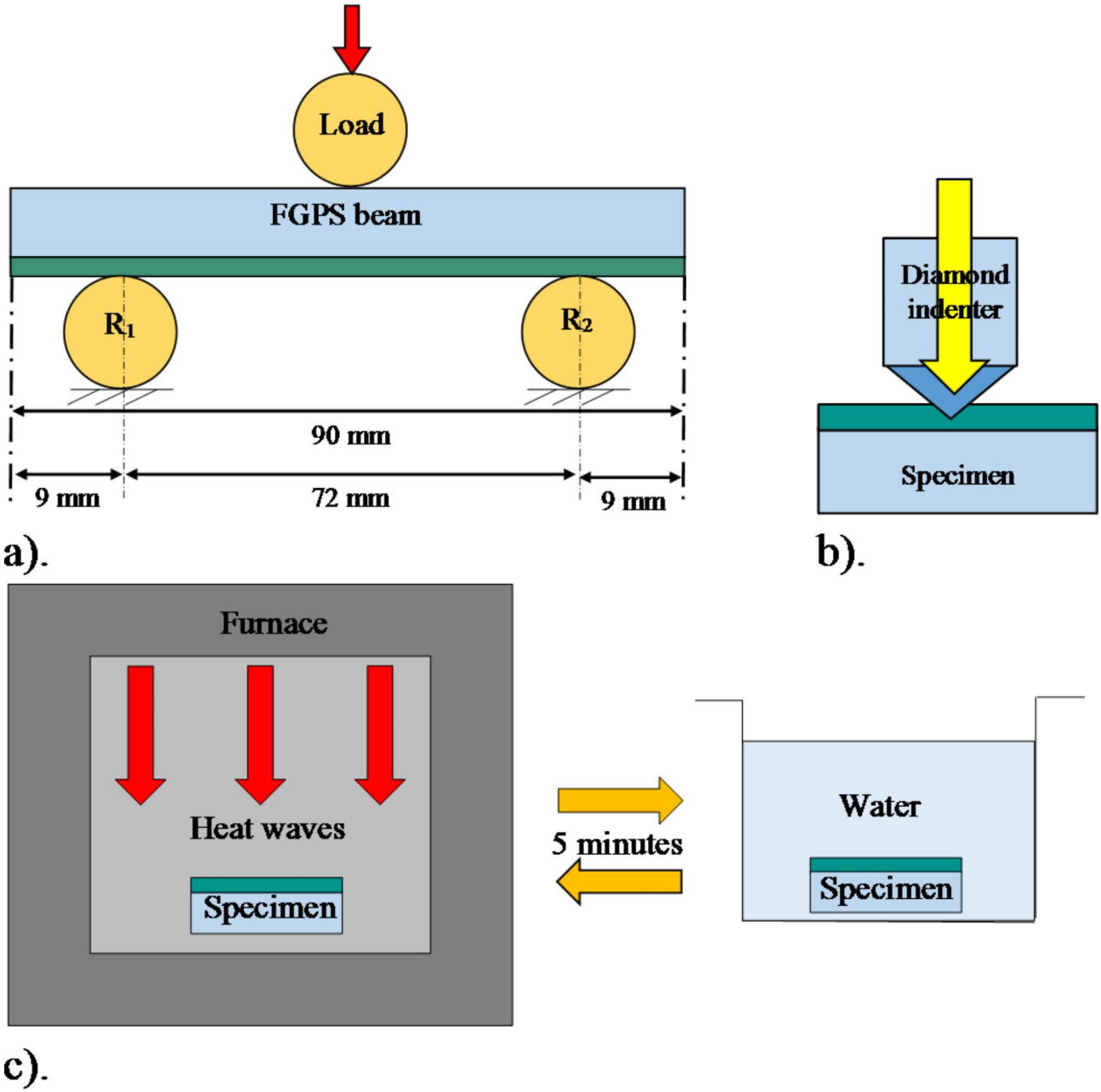

Fig. 3. Mechanical tests: (**a**) Three point bending. (**b**) Microhardness test. (**c**) Thermal shock test.

$$\rho_z = V_c \rho_c + V_m \rho_m \tag{4}$$

Individual layers in the functionally graded coating are treated as metal-matrix composites and their Young's modulus E is calculated based on the TTO model[32–34]. The composite's Young's modulus was computed using the following expression, Eq. (5), through mean value of stress and strain and Hook's law.

$$E = \left[V_m E_m \frac{E_c + q}{E_m + q} + E_c (1 - V_m) \right] / \left[V_m \frac{E_c + q}{E_m + q} + (1 - V_m) \right] \tag{5}$$

$$q = \frac{\sigma_c - \sigma_m}{|\epsilon_c - \epsilon_m|} \tag{6}$$

The stress-strain transfer rate q is described by Eq. (6) which is dependent on the composite's microstructural bonding, volume fraction and material composition based on grain shape, size and orientation. The q value for the Al/SiC FG coating used in the current investigation is 4.8 GPa[33].

$$\frac{\sigma_Y}{\sigma_0} = \frac{E_c}{E_m} \times \frac{q + E_m}{q + E_c}(1 - V_m) + V_m \tag{7}$$

The TTO model assumes that as the metal components in the FG coating begin to yield, the coating will reach its yield point. The FG coating's yield stress σ_Y, is computed from Eq. (7), based on the metal yield stress σ_0.

$$\frac{\epsilon}{\epsilon_Y} = \frac{E}{E_m}\frac{q + V_m E_c}{q + E_c}\frac{\sigma_0}{\sigma_Y}\left(\frac{\sigma_m}{\sigma_0}\right)^{n_0} + \frac{\sigma_m}{\sigma_Y}\frac{EV_c}{q + E_c} \tag{8}$$

$$\frac{\sigma}{\sigma_Y} = \frac{1}{E_m}\frac{qV_c E_c}{q + E_c}\frac{\sigma_0}{\sigma_Y}\left(\frac{\sigma_m}{\sigma_0}\right)^{n_0} + \frac{\sigma_m}{\sigma_Y}\frac{qV_m + E_c}{q + E_c} \tag{9}$$

The Eqs. (8) and (9) describes the flow curves of FG coating, where n_0 is the hardening exponent 7.37 taken from the literature[33].

The most extensively used nonlinear plasticity material model is the Johnson-Cook (JC) model when metals are subjected to temperature, extreme strains and higher strain rates. The flow stress as per the JC model, is given by Eq. (10), where *m* is the thermal softening coefficient, *T* is the temperature, $\frac{\dot{\epsilon}}{\dot{\epsilon}_0}$ is the non-dimensional plastic strain rate, *C* the strain rate strengthening coefficient,ϵ the plastic strain, *B* the strain hardening constant and *A* represents the yield stress. The stress as a function of strain is given in the first bracket, the influence of strain rate is represented by the second bracket and the effect of temperature is depicted in the third bracket.

$$\bar{\sigma} = (A + B\epsilon^p)\left(1 + Cln\frac{\dot{\epsilon}}{\dot{\epsilon}_0}\right)\left[1 - \left(\frac{T - T_{Room}}{T_{Melt} - T_{Room}}\right)^m\right] \tag{10}$$

The JC damage model defines the damage of an element during the numerical simulation in Eq. (11), where $\overline{\epsilon_f}$ is the equivalent strain at failure (Eq. (12)) and $\Delta\overline{\epsilon_f}$ is the equivalent failure strain increment, which is increased with each analysis step. The relevant failed element is automatically eliminated from the computation when the damage parameter D exceeds unity, indicating that failure has occurred.

$$D = \sum\left(\frac{\Delta\bar{\epsilon}}{\overline{\epsilon_f}}\right) \tag{11}$$

$$\overline{\epsilon_f} = \left[D_1 + D_2 exp\left(D_3\frac{\sigma_m}{\bar{\sigma}}\right)\right]\left[1 + D_4 ln\left(\frac{\dot{\epsilon}}{\dot{\epsilon}_0}\right)\right]\left[1 + D_5\left(\frac{T - T_{Room}}{T_{Melt} - T_{Room}}\right)\right] \tag{12}$$

where $\frac{\sigma_m}{\bar{\sigma}}$ is the pressure-stress ratio, D_1, D_2, D_3, D_4 and D_5 represents the damage constants.

Finite element model

The FGPS plate's finite element modeling and simulation under high velocity impact at various temperatures was performed using the nonlinear explicit finite element code, LS-DYNA. All the numerical simulations were performed at the same impact energy 260 J and their equivalent impact velocity is 88 m/s. The simulations were run at seven (298 K, 323 K, 373 K, 473 K, 573 K, 673 K, and 773 K) different temperatures with the same impact energy to have a better understanding of the effect of temperature. The FGPS plate of 100 mm × 100 mm size is modelled with solid element (SOLID 164) having 9 degrees of freedom (translation, velocity, acceleration) as in Fig. 4(a). The average coating thickness of the Al/SiC four-layered FG coating was 232.8 µm from the cross sectional SEM analyses. Since the interface between the layers was indistinguishable in SEM analysis, each layer thickness was assumed to be 0.05 mm for the modelling of the coating and the cross-sectional view of the FG coated model is represented in Fig. 4(b). To increase the accuracy of the outcomes, the enhanced central zone meshing technique is used and a temperature was applied to all the nodes of the FGPS plate. To avoid contact instabilities, the steel projectile (Fig. 4(c)) is modelled 1 mm above the FGPS plate and an impact velocity was assigned to all the nodes of the projectile. Mesh convergence studies were initially performed and determined the appropriate mesh sizes for various cases and the Table 1 provides the total number of elements and mesh size employed in the finite element analysis.

The contact algorithm is essential for defining the contact between the parts during the impact analysis and it automatically updates the contact with the subsequent new surface when the element reaches the failure strain and deleted. The contact between the FGPS plate and the projectile is assigned by the ERODING_SURFACE_TO_SURFACE contact with static and dynamic friction coefficients of 0.47 and 0.38. For this set of contact algorithms, a formulation that relies on pinball ball based segment was used. The steel projectile is modeled using the MAT_PLASTIC_KINEMATIC material model, whereas the base plate aluminum 6061-T6 is modeled using the JOHNSON_COOK damage model. PIECEWISE_LINEAR_PLASTICITY is the material model utilized for modeling the layers of FG coating. The THERMAL_ISOTROPIC material model is employed for the FGPS plate that inputs the isotropic thermal property. The AUTOMATIC_SURFACE_TO_SURFACE is a two-way contact algorithm that is specifically used for impact analysis as a soft contact, with the slave node checking for penetration first, followed by the master node. In order to prevent the structure from moving during impact, the FGPS plate was clamped 10 mm at each edge, fixing all of the nodes' degrees of freedom within that boundary. For the thermo-structural coupled analysis, the solver is set to be a symmetric direct solver. The solver must assess the structural and thermal solutions in two distinct numerical phases for each global step of the solution. The thermal time step is often set to 0.01 ms, whereas the structural time step is typically set to 0.001 ms. Table 2

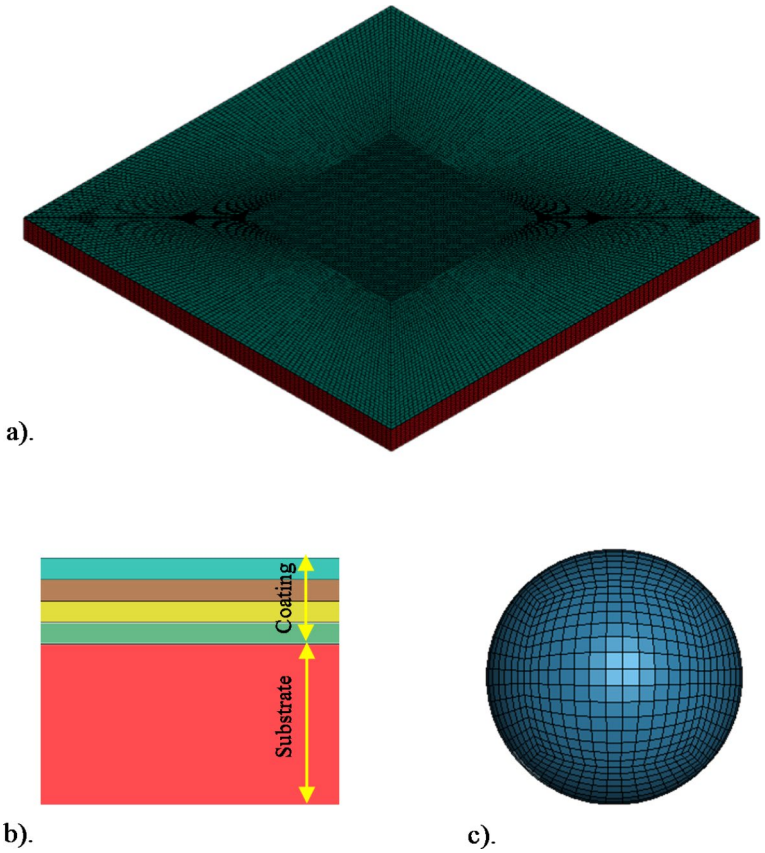

Fig. 4. Finite element model: (**a**) FGPS plate. (**b**) Detailed view of FGPS. (**c**) Spherical Projectile.

Structure	Element type	Number of elements	Mesh size (mm)
Projectile	SOLID-164	23,625	0.8–1.6
Al/SiC coatings	SOLID-164	76,800	0.5–1.2
Base plate	SOLID-164	192,000	0.5–1.2
Total	-	292,425	-

Table 1. Details of FGPS finite element modelling.

	Density, kg/m^3	Young's modulus (GPa)	Yield stress (MPa)	Poisson's ratio	Failure strain	Specific heat (J/(KgK))	Thermal conductivity (W/(mK))	Melting temperature (K)
Steel AISI 4340	7850	200	970	0.29	0.77	450	44.5	1700
Al 6061	2702	67	95	0.33	0.74	875	220	650
SiC	3100	302	-	0.17	0.01	750	120	3003
Al 6061-T6	2660	70.3	-	0.28	-	896	167	650

Table 2. Material properties of FGPS components[24,35–39].

lists the material characteristics of the FGPS plate and projectile. Table 3 provides the JC model's plasticity and failure constants.

Results and discussion

High velocity impact test

Validation of the numerical model

Numerical simulations were performed on the FGPS plate at 573 K and 260 J impact energy. For the purpose of validating the finite element model, the damage behavior was then compared with the experimental findings. Under this impact scenario, the FGPS plate experiences a visible circular dent at the center and undergoes

Material	D1	D2	D3	D4	D5	A (MPa)	B (MPa)	C	*p*	m
Al 6061-T6	-0.77	1.45	-0.47	0	1.6	270	195	0.02	0.3	1.34

Table 3. Damage parameters and plasticity constants of JC model[24,35].

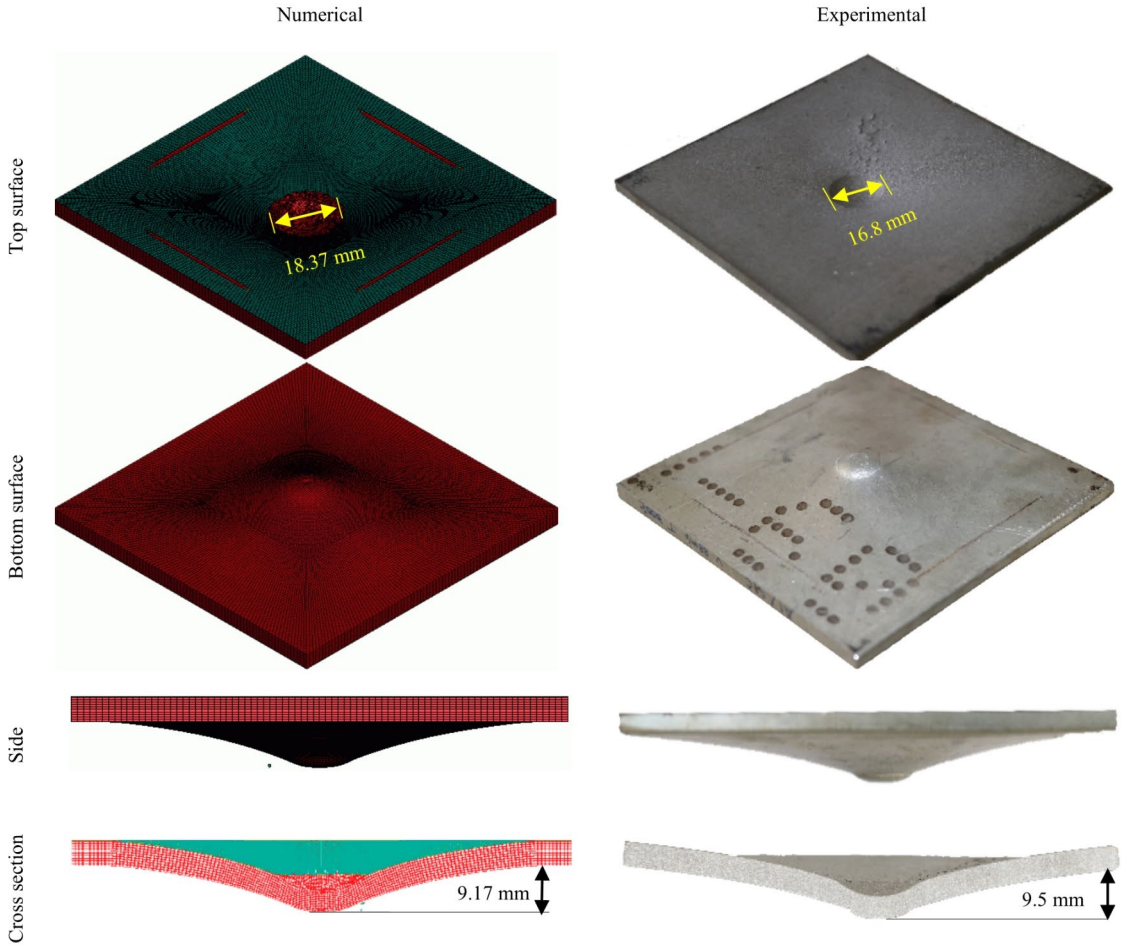

Fig. 5. Comparison between the numerical and experimental results under 260 J impact at 573 K.

global bending, as shown in Fig. 5. The central deflection obtained through the numerical simulation and experimental is 9.17 mm and 9.5 mm, respectively. Also, the dent diameter determined by numerical simulation and experiment is 18.37 mm and 16.8 mm, respectively. Thus, the experimental results seem to be in good agreement (90.65%) with the computational findings, thereby validating the numerical model. The remaining 9.35% of the difference in the data is caused by geometric misalignments and the porosity of the FG coating.

Effect of temperature

Numerical simulations were performed using a same impact energy of 260 J at 298 K, 323 K, 373 K, 473 K, 573 K, 673 K, and 773 K to gain an additional insights into the impact dynamics at elevated temperatures. The structural response of the FGPS plate under a 260 J impact at various temperatures is shown in Fig. 6. An indentation was observed at the center and damages are seen at the four edges due to the fixed boundary condition used to replicate the fixture. As the temperature increases, the central deflection increases and eventually perforates at 773 K. When the impactor touches the FGPS plate, the impactor's kinetic energy starts to dissipate in the plate as elastic and plastic energy. The time history of energy absorption by the plate during the elastic and plastic deformation is plotted in Fig. 7(a). The rate of energy absorption decreases with increasing temperature due to the plate's stiffness decreases with increasing temperature. Initially, all the energy absorption curves (except 773 K) of the FGPS plate increase with time and reach 260 J, which is equal to the incident impact energy

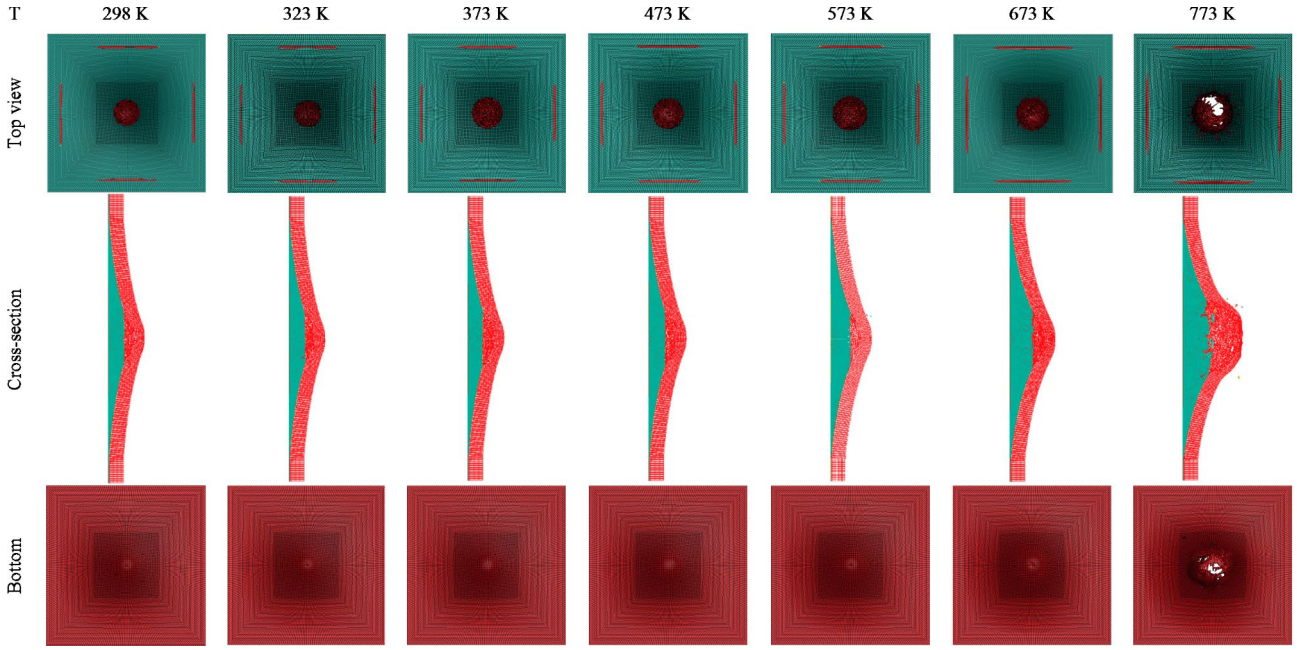

Fig. 6. High velocity impact under various temperatures.

of the impactor. During the process, the plate undergoes global bending and stores the energy as elastic and plastic deformations. Then the elastically stored energy is expended as rebound of the impactor and the plate, as a result of which the energy dropped from 260 J and remained constant thereafter. At 773 K, the impactor starts to perforate the structure due to the reduced stiffness and hence the energy absorption of the FGPS plate is minimal. The velocity of the impactor reduces from 88 m/s to zero and starts to rebound from the plate depending on the elastically stored energy (Fig. 7(c)). The rebound velocity of the impactor is maximum at room temperature due to its increased stiffness and it starts to reduce for the higher temperature impact simulations.

As the impactor touches the FGPS plate, the contact force increases rapidly, reaches a maximum value and eventually drops to zero (Fig. 7(b)). The peak contact force decreases with temperature and the corresponding peak contact time increases. The reduction in the peak contact force at higher temperatures may be attributed to the stiffness reduction based on temperature. The displacement at different temperatures along the cross section (sectioned at the center) is depicted in Fig. 7(d). The displacement increases gradually from the edge and it reaches its highest value at the center of the FGPS plate where the projectile impacts. The central deflection is nearly identical for 298 K, 323 K, and 373 K and it increases drastically beyond 373 K. The peak contact force, central deflection and dent diameter at various temperatures under the impact load are listed in Table 4. From the impact simulations under various temperatures, it is observed that the stiffness reduction at higher temperatures results in decreased peak contact force, decreased rebound velocity and increased central deflection.

The experiments conducted at room temperature[3] and 573 K are compared to understand the impact damage behavior of coatings, as shown in Fig. 8. Delamination of the coating happens when the impact test is conducted at room temperature because the transient stress waves traverse back and forth at a higher velocity along the thickness. Interestingly, it is observed that in the impact test conducted at 573 K, the sample does not undergo delamination; rather, the coating sticks all around the surface. SiC becomes more stable as the temperature rises, but increased thermal energy causes the Al atoms in the lattice to vibrate more, making dislocations easier to move. The enhanced atomic vibrations weaken the bonds between the atoms. This can result in reduced stiffness, reduced yield strength, and increased ductility. Due to the reduced stiffness, the stress waves travel at a comparatively lower velocity and hence no delamination occurs.

Micro-morphological study of Al/SiC FGPS coating

The cross-sectional morphology of the FGPS coating, coating-substrate interface and coating thickness at nine different locations are shown in Fig. 9. The coating thickness, consisting of four functionally graded layers with varying compositions, ranges from 215.17 μm to 247.3 μm, having an average of 232.8 μm. The cross-sectional micro-morphology shows that the FGPS coating and the aluminum substrate have strong adherence. The Al and SiC particles are visible on the FGPS plate's top surface micro-morphology (Fig. 10). The high-temperature plasma melts the injected powder particles and forms molten splats on the plate. The molten splats have spread several micrometers, which indicates excellent bonding between the particles. Additionally, a few non-melted particles strike the molten splats at a higher velocity and create waviness in some locations, which leads to the roughness increment. The un-melted particles create porosity on the surface of the coating. The porosity analysis was performed on five different locations of the FGPS surface using an optical microscope at 100 X magnification and the findings are presented in Fig. 11. The porosity content varies from 1.19 to 1.69% and the average porosity content was found to be 1.35%.

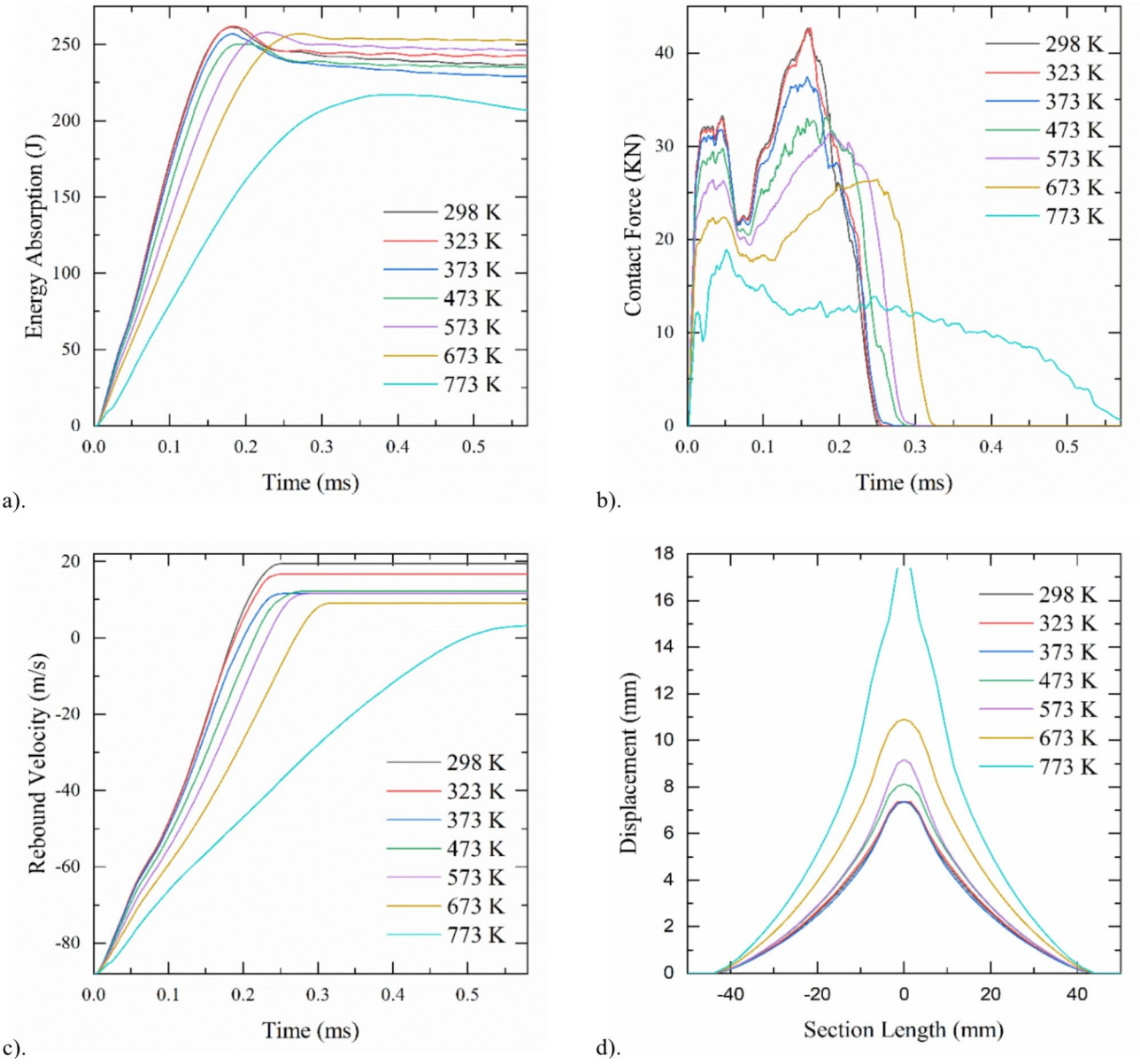

Fig. 7. Effect of temperature on the FGPS plate: (**a**) Energy absorption. (**b**) Contact force history. (**c**) Rebound velocity. (**d**) Displacement along the cross section.

Temperature (K)	Central deflection (mm)	Dent diameter (mm)	Peak force (KN)
298	7.36	16.77	42.63
323	7.36	16.77	42.70
373	7.36	17.77	37.44
473	8.11	18.29	32.94
573	9.17	18.37	31.45
673	10.9	19.18	26.49
773	Penetration	25.44	18.91

Table 4. Central deflection, dent diameter and peak contact force evolution at elevated temperatures.

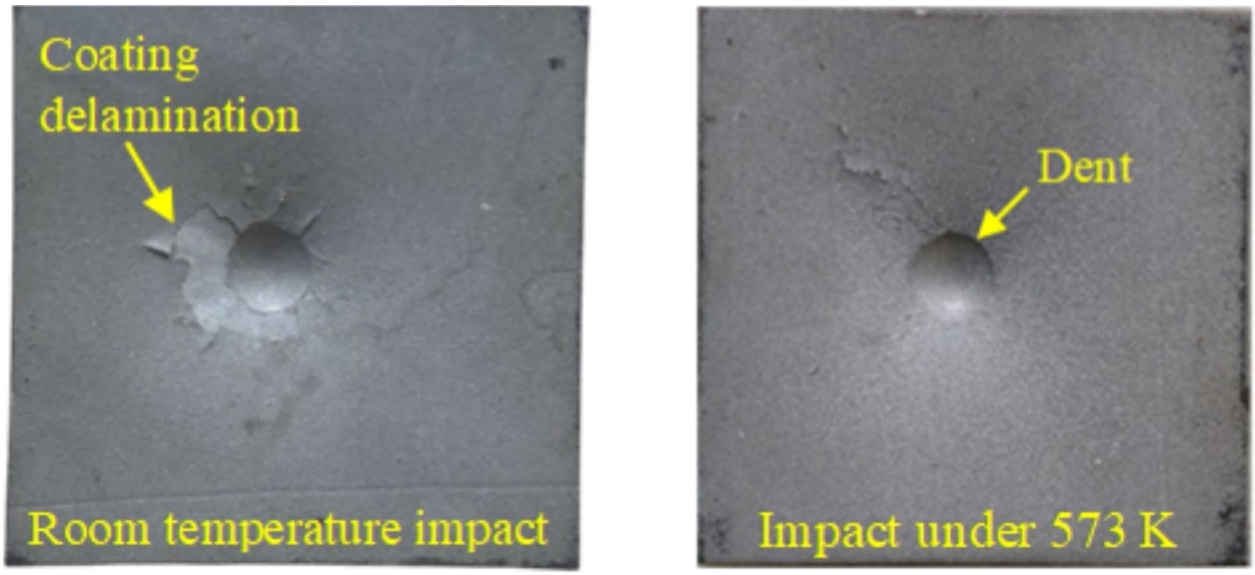

Fig. 8. Comparison between the room temperature impact test and impact under 573 K.

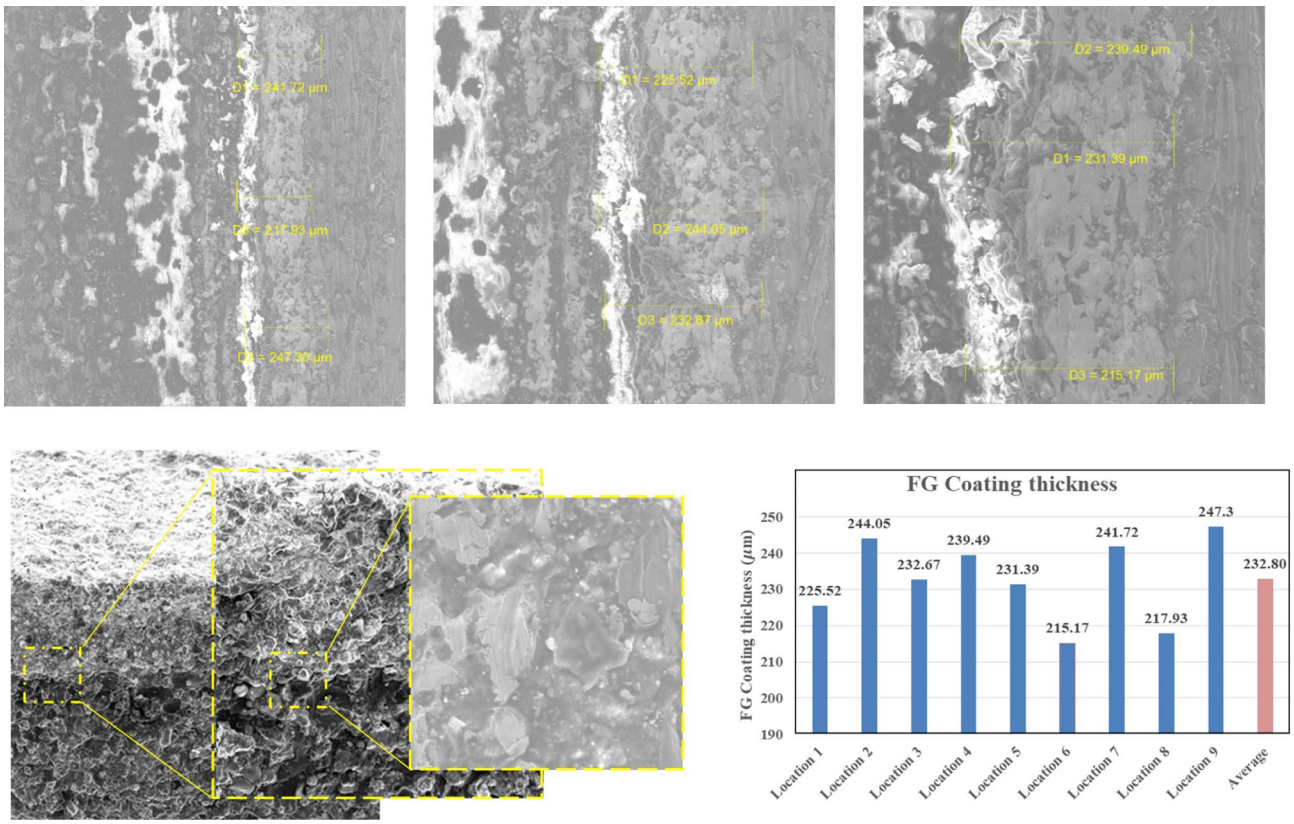

Fig. 9. Cross-sectional morphology of the FGPS coating.

Mechanical properties of FGPS sample

Under uniaxial tension, the aluminium substrate undergoes ductile fracture in the shape of a cup-cone, whereas the FG coating experiences brittle fracture (Fig. 12(a)). The FG coating delaminates (at 5% strain) only in the necking region of the substrate, while the other areas, including the gripping region, remain undamaged. The yield and ultimate strength of the FGPS specimen are 253 MPa and 278 MPa, respectively. The complete failure of the specimen occurred at 15% of the strain and the corresponding stress is 241 MPa. Figure 12(b) illustrates the flexural behavior under the three-point bend test. A sudden brittle fracture occurred at 5.55% of the strain

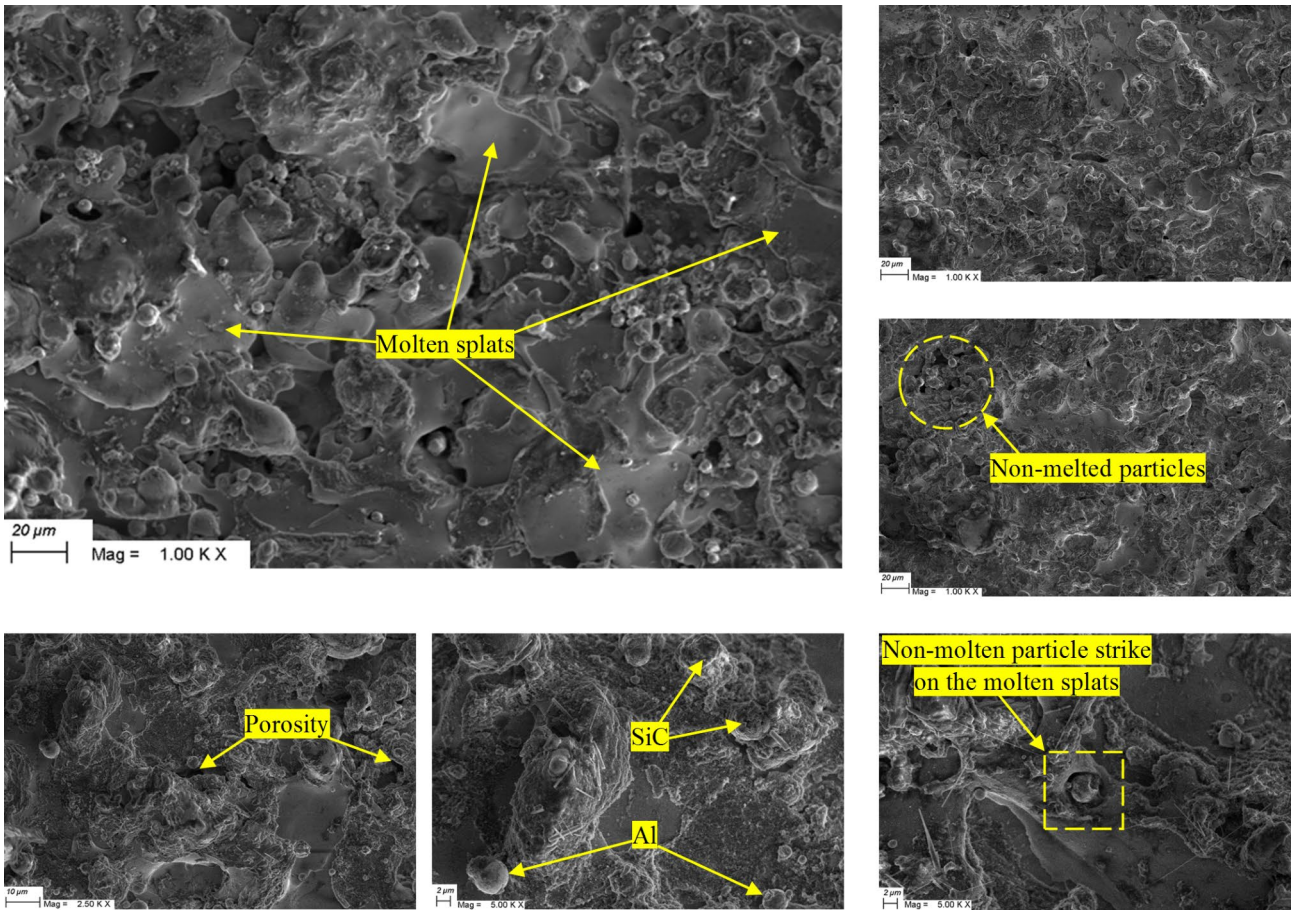

Fig. 10. Top surface morphology of FGPS coating.

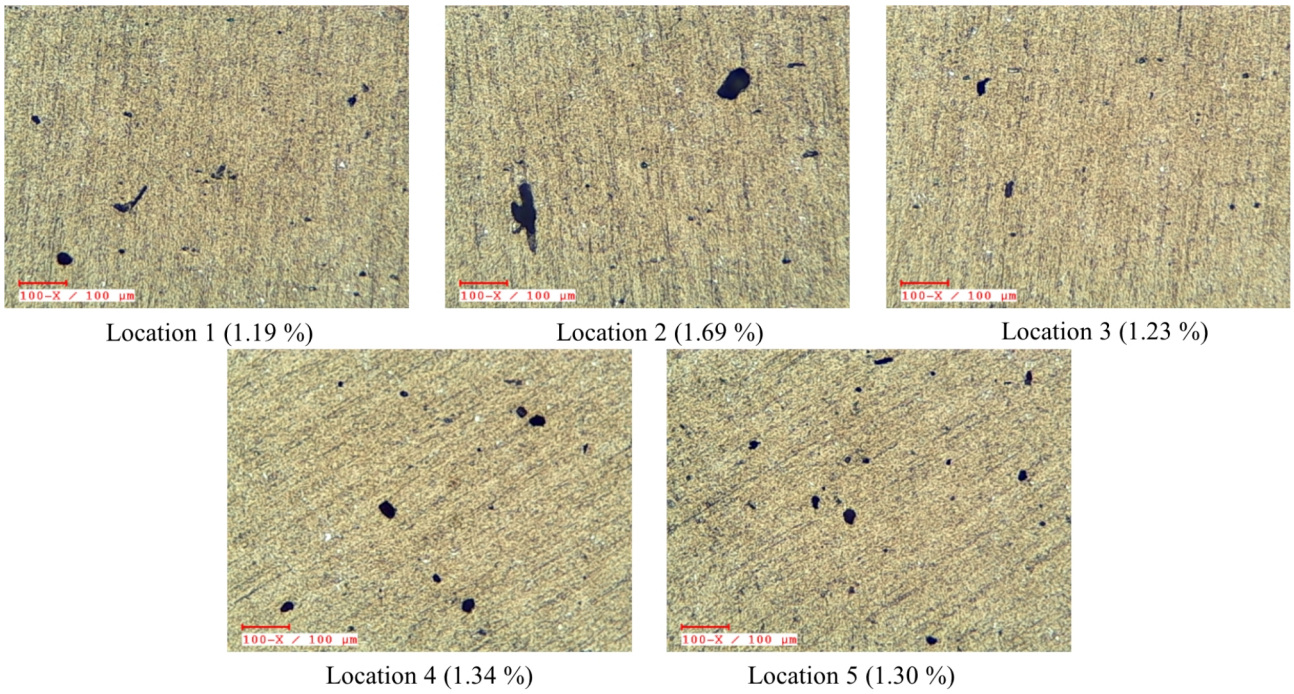

Fig. 11. Porosity content on the FGPS coating's top surface.

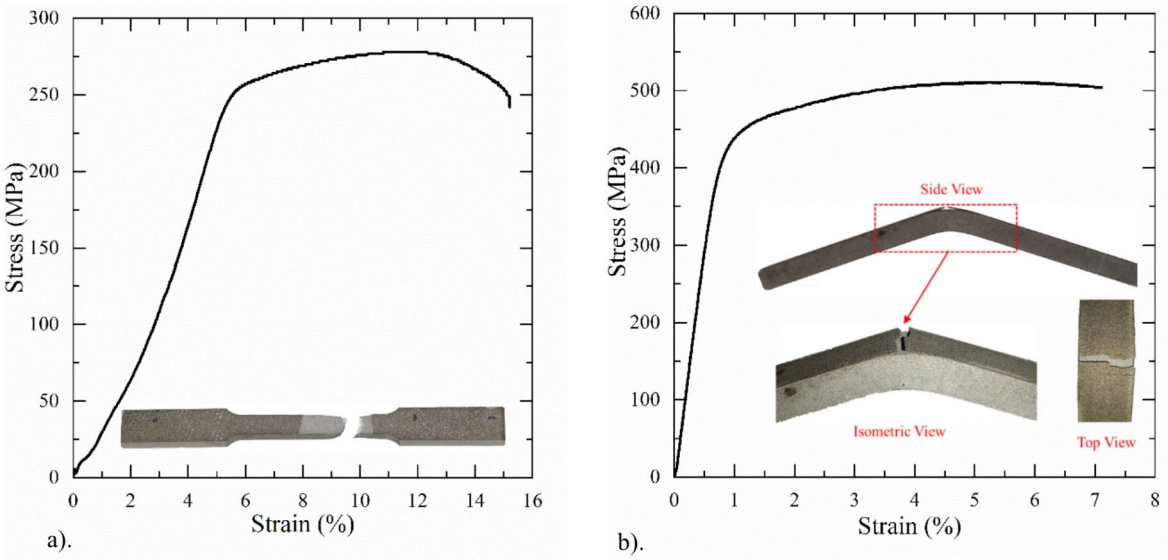

Fig. 12. Stress-strain plot: (**a**) Tensile test. (**b**) Flexural test.

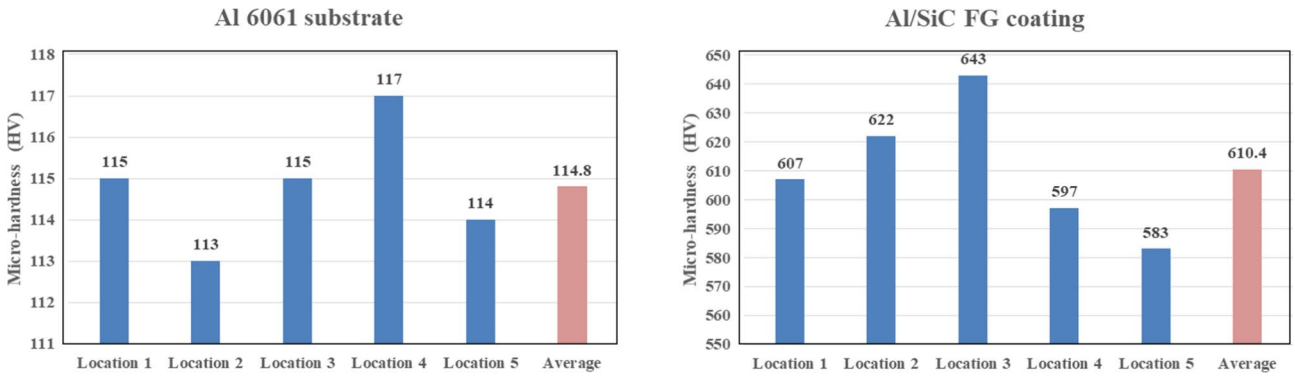

Fig. 13. Microhardness of Al 6061 substrate and FGPS coated plate.

(corresponding flexural strength is 511 MPa), during which the FG coating delaminates at the center where load is applied. During this event, a fracture sound was observed due to the crack formation. The brittle fracture clearly indicates that the coating consists of ceramic-rich content.

Vickers hardness was measured at five distinct locations on the FGPS coating surface and it ranges from 583 HV to 643 HV (Fig. 13). For the same loading and dwell time, the microhardness of the non-coated surface (aluminium substrate) was measured and it ranges from 113 HV to 117 HV. The average Vickers hardness of the FGPS coating and non-coated aluminium surface was measured to be 610 HV and 115 HV respectively. The hardness of the FGPS sample was five times better than the non-coated sample.

The non-coated aluminum substrate's surface roughness is shown in Fig. 14(a). Using the surface roughness tester, the average roughness (R_a) is found to be 0.28 $\mu\, m$ and the maximum depth of the roughness (R_z) is 1.79 $\mu\, m$, which shows that the non-coated aluminium sample surface finishing is smooth. The FGPS coated sample's surface roughness is shown in Fig. 14(b). The plot shows increased fluctuation, which is a sign that the top layer contains some porosity. The non-uniform dispersion of the coating in the top layer is mostly caused by the rapidly accelerated, non-melted particles that were struck onto the molten splats of the third layer. The average roughness (R_a) is found to be 3.9 $\mu\, m$ and the maximum depth of the roughness (R_z) is 21.54 $\mu\, m$, indicating that the FGPS coating's surface is noticeably rougher than the non-coated aluminum substrate.

The response of the FGPS sample (10 mm × 10 mm) during the thermal shock test is shown in Fig. 15. No delamination was observed up to the 12th cycle. After the 16th cycle, the delamination starts at the corner of the FGPS plate due to the adhesive failure. At the 20th cycle, a large sudden failure of coating occurs during water

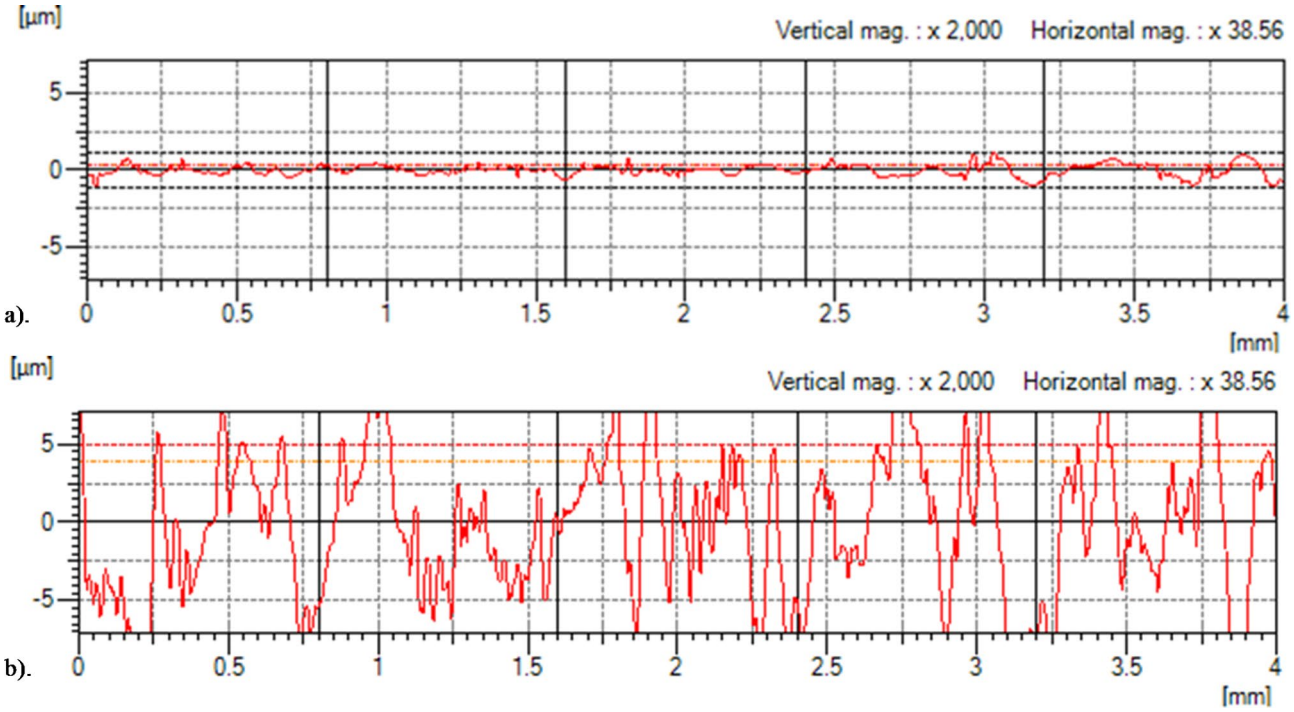

Fig. 14. Graphical plot of Surface roughness: (**a**) Aluminium substrate; (**b**) FGPS coated plate.

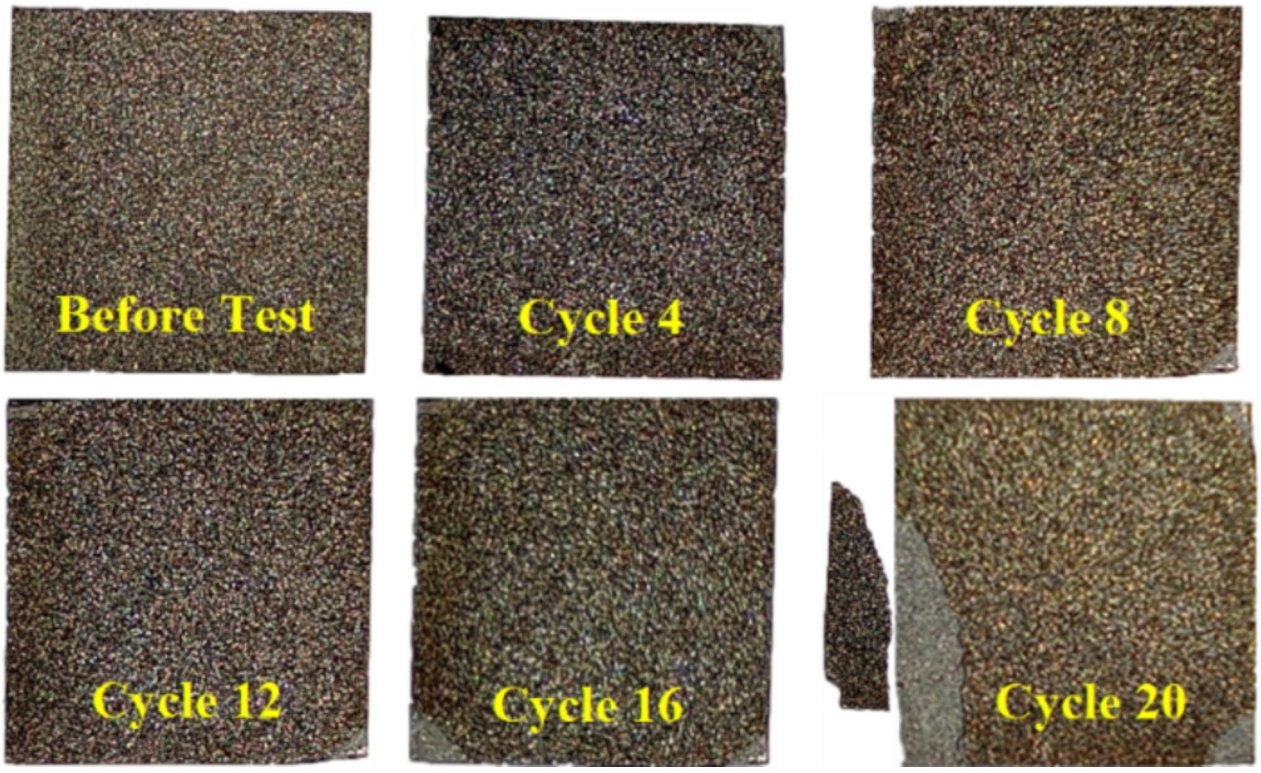

Fig. 15. FGPS subjected to thermal shock test.

quenching at room temperature. This is due to the fact that the variation between the substrate's and coating's thermal expansion coefficients causes the material to expand and contract at different rates. When the coated sample is kept inside the muffle furnace, the metal substrate heats up and expands faster than the ceramic rich coating (FGPS coating). During the water quenching process, the aluminium cools rapidly due to the sudden

temperature drop. As a result of this effect, residual stress is developed in the bond coat and hence adhesive failure occurs.

Conclusions

FGPS coating was performed with four layers of Al/SiC on the aluminium 6061-T6 substrate and mechanical properties were evaluated to understand the characteristics of the coating initially. The high-velocity impact experiments were subsequently carried out with a single stage gas gun at elevated temperatures in order to understand the coating's damage behavior. In addition, computational simulations were carried out to understand the impact dynamics of the FGPS plate at various temperatures. The computational and experimental results are match well in terms of damage behavior, central deflection and dent diameter. The impactor's kinetic energy begins to dissipate as elastic and plastic energy as it comes into contact with the FGPS plate, causing the plate to deform. The rate of energy absorption decreases with increasing temperature because the plate's stiffness decreases with increasing temperature. From the high velocity impact simulations under various temperatures, it is observed that the stiffness reduction at higher temperatures results in decreased peak contact force, decreased rebound velocity and increased central deflection. At room temperature impact test, coating delamination occurs due to the transient stress waves traverse back and forth at a higher velocity along the thickness. It is worth noting that the impact test conducted at 573 K does not undergo delamination; rather, the coating sticks all around the surface. As the temperature increases, due to the reduced stiffness, the stress waves travel at a comparatively lower velocity hence no delamination occurs. The molten splats observed through micro-morphological study have spread several micrometers, which indicates excellent bonding between the particles. The thickness of the FGPS coating varies from 215.17 μm to 247.3 μm and the average coating thickness was found to be 232.8 μm. According to the porosity analysis, the coating has an average porosity content of 1.35% due to the unmelted particles. The average Vickers hardness of the FGPS coating and non-coated aluminium surface was measured to be 610 HV and 115 HV, respectively. The hardness of the FGPS sample was five times better than the non-coated sample. The average roughness is found to be 3.9 μm and the maximum depth of the roughness is 21.54 μm indicating that the FGPS coating's surface is significantly rough. As a result, the specimen level data elucidates material behavior under controlled environments, aiding engineers in analyzing failure mechanisms to enhance failure-resistant structural designs for space applications. The present research is crucial for identifying materials capable of withstanding temperature variations in space applications. Especially, the FGPS coating can be used as thermal and oxidation resistant coating for the structures that undergo very high temperatures. The present analysis can be extended to study the effect of imperfections on the damage behavior under high velocity impact.

Data availability

The datasets used and/or analyzed during the current study are available from the corresponding author upon reasonable request.

Received: 18 August 2024; Accepted: 22 November 2024
Published online: 25 November 2024

References

1. Saleh, B. et al. 30 Years of functionally graded materials: An overview of manufacturing methods, applications and future challenges. *Compos. Part B Eng.* **201**, 108376 (2020).
2. Han, Q., Wang, Z., Nash, D. H. & Liu, P. Thermal buckling analysis of cylindrical shell with functionally graded material coating. *Compos. Struct.* **181**, 171–182 (2017).
3. Muniraj, D. & Sreehari, V. M. Damage assessment of sandwich structures with Al/SiC functionally graded plasma sprayed faceplates subjected to single and repeated impacts. *Compos. Struct.* **287**, 115369 (2022).
4. Deng, C., Kim, H. & Ki, H. Fabrication of functionally-graded yttria-stabilized zirconia coatings by 355 nm picosecond dual-beam pulsed laser deposition. *Compos. Part B* **160**, 498–504 (2019).
5. Lin, C.-Y. Production of silicon carbide Al 2124 alloy functionally graded materials by mechanical powder metallurgy technique. *Powder Metall.* **42**, 29–33 (1999).
6. Smith, M. F. Plasma spray deposition-a review of technology and research opportunities. *AIAA 23rd Plasmadynamics Lasers Conf. 1992* (1992) https://doi.org/10.2514/6.1992-3013.
7. Ghara, T. & Bandyopadhyay, P. P. Understanding the role of in-flight particle temperature and velocity on the residual stress depth profile and other mechanical properties of atmospheric plasma sprayed Al2O3 coating. *J. Eur. Ceram. Soc.* **42**, 4353–4368 (2022).
8. Hussain, S., Shah, Z. A., Sabiruddin, K. & Keshri, A. K. Characterization and tribological behaviour of Indian clam seashell-derived hydroxyapatite coating applied on titanium alloy by plasma spray technique. *J. Mech. Behav. Biomed. Mater.* **137**, 105550 (2023).
9. Willson, R. Low pressure plasma spraying of highly dense NiCrAlY-CuCrAl coating system on copper alloy substrates. *Collect. Tech Pap. AIAA/ASME/ASCE/AHS/ASC Struct. Struct. Dyn. Mater. Conf.* **5**, 4408–4420 (2007).
10. Zhang, X. et al. Interface evolution of Si/Mullite/Yb2SiO5 PS-PVD environmental barrier coatings under high temperature. *J. Eur. Ceram. Soc.* **40**, 1478–1487 (2020).
11. Seifert, S., Kleiman, J. I. & Heimann, R. B. Thermal optical properties of plasma-sprayed mullite coatings for space launch vehicles. *J. Spacecr. Rockets* **43**, 439–442 (2006).
12. Khor, K. A. & Gu, Y. W. Thermal properties of plasma-sprayed functionally graded thermal barrier coatings. *Thin Solid Films* **372**, 104–113 (2000).
13. Mohammadzaki Goudarzi, Z., Valefi, Z., Zamani, P. & Taghi-Ramezani, S. Comparative investigation of the effect of composition and porosity gradient on thermo-mechanical properties of functionally graded thick thermal barrier coatings deposited by atmospheric plasma spraying. *Ceram. Int.* **48**, 28800–28814 (2022).
14. Thirumalaikumarasamy, D., Kamalamoorthy, K. S. & Visvalingam, V. B. Effect of experimental parameters on the micro hardness of plasma sprayed alumina coatings on AZ31B magnesium alloy. *J. Magnes. Alloy.* **3**, 237–246 (2015).
15. Wu, Y., Lin, P., Wang, Z. & Li, G. Microstructure and microhardness characterization of a Fe-based coating deposited by high-velocity oxy-fuel thermal spraying. *J. Alloys Compd.* **481**, 719–724 (2009).

16. Yongzhong, W. & Donghui, Z. Electrochemical corrosion behaviors and microhardness of laser thermal sprayed amorphous AlCrNi coating on S275JR steel. *Opt. Laser Technol.* **118**, 115–120 (2019).
17. Habib, K. A. *et al.* Effects of thermal spraying technique on the remelting behavior of NiCrBSi coatings. *Surf. Coatings Technol.* **444**, (2022).
18. Patel, K., Doyle, C. S., Yonekura, D. & James, B. J. Effect of surface roughness parameters on thermally sprayed PEEK coatings. *Surf. Coatings Technol.* **204**, 3567–3572 (2010).
19. Patibanda, S. et al. Mechanical behavior of freestanding 8YSZ thin films under tensile and bending loads. *Surf. Coatings Technol.* **393**, 125771 (2020).
20. Wang, L., Shi, J., Gao, J. & Yan, D. Influence of tungsten carbide particles on resistance of alumina matrix ceramics to thermal shock. *J. Eur. Ceram. Soc.* **21**, 1213–1217 (2001).
21. Loghman-estarki, M. R., Shoja, R. & Edris, H. Life time of new SYSZ thermal barrier coatings produced by plasma spraying method under thermal shock test and high temperature treatment. *Ceram. Int.* **40**, 1405–1414 (2014).
22. Huang, W. et al. Optimization of mechanical properties and thermal shock resistance of LaPO4/8YSZ thick composite coatings via plasma spraying. *J. Alloys Compd.* **913**, 165256 (2022).
23. Sahu, S., Pada Mondal, D., Dass Goel, M. & Zahid Ansari, M. Finite element analysis of AA1100 elasto-plastic behaviour using Johnson-Cook model. *Mater. Today Proc.* **5**, 5349–5353 (2018).
24. Chocron, S., Erice, B. & Anderson, C. E. A new plasticity and failure model for ballistic application. *Int. J. Impact Eng.* **38**, 755–764 (2011).
25. Krishnan, K., Sockalingam, S., Bansal, S. & Rajan, S. D. Numerical simulation of ceramic composite armor subjected to ballistic impact. *Compos. Part B Eng.* **41**, 583–593 (2010).
26. Sinha, S. K., Czarnecki, G. J. & Hinrichsen, R. L. Dynamic analysis of damage to aircraft propulsion system impacted by exploding missile. *J. Aircr.* **50**, 1526–1532 (2013).
27. Rhymer, J., Kim, H. & Introduction, I. Composite Panels Impacted by High Velocity Ice. *Collect. Tech. Pap. - AIAA/ASME/ASCE/AHS/ASC Struct. Struct. Dyn. Mater. Conf.* 1–11 (2012).
28. Li, Y., Yang, Y., Li, J., Wang, B. & Liao, Y. Experimental-numerical analysis of failure of adhesively bonded lap joints under transverse impact and different temperatures. *Int. J. Impact Eng.* **140**, 103541 (2020).
29. Liu, H., Ding, S. & Ng, B. F. Impact response and energy absorption of functionally graded foam under temperature gradient environment. *Compos. Part B Eng.* **172**, 516–532 (2019).
30. Lee, C. & Kim, J. Aero-thermoelastic stability and nonlinear flutter analysis of functionally graded panels. *J. Compos. Mater.* **47**, (2013).
31. Gunes, R., Hakan, M., Apalak, M. K. & Reddy, J. N. Numerical investigation on normal and oblique ballistic impact behavior of functionally graded plates. *Mech. Adv. Mater. Struct.* **28**, 2114–2130 (2021).
32. Gunes, R., Aydin, M., Kemal Apalak, M. & Reddy, J. N. Experimental and numerical investigations of low velocity impact on functionally graded circular plates. *Compos. Part B Eng.* **59**, 21–32 (2014).
33. Zhu, B. & Cai, Y. J. A strain rate-dependent enhanced continuum model for elastic-plastic impact response of metal-ceramic functionally graded composites. *Int. J. Impact Eng.* **133**, (2019).
34. Zafarmand, H. & Kadkhodayan, M. Nonlinear material and geometric analysis of thick functionally graded plates with nonlinear strain hardening using nonlinear finite element method. *Aerosp. Sci. Technol.* **92**, 930–944 (2019).
35. Sun, G., Chen, D., Wang, H., Hazell, P. J. & Li, Q. High-velocity impact behaviour of aluminium honeycomb sandwich panels with different structural configurations. *Int. J. Impact Eng.* **122**, 119–136 (2018).
36. Arslan, K., Gunes, R., Apalak, M. K. & Reddy, J. N. Experimental tests and numerical modeling of ballistic impact on honeycomb sandwich structures reinforced by functionally graded plates. *J. Compos. Mater.* **51**, 4009–4028 (2017).
37. Li, S. et al. Optimization of milling aluminum alloy 6061–T6 using Modified Johnson-Cook model. *Simul. Model. Pract. Theory* **111**, 102330 (2021).
38. Yin, J. et al. Nd: YAG laser ablation of aluminum alloy 6061 before and after silicon dioxide coating. *J. Alloys Compd.* **877**, 160329 (2021).
39. Sedighi, M., Afshari, D. & Nazari, F. Investigation of the effect of sheet thickness on residual stresses in resistance spot welding of aluminum sheets. *Proc. Inst. Mech Eng. Part C J. Mech. Eng. Sci.* **232**, 621–638 (2018).

Acknowledgements

This research work was supported by the Science and Engineering Research Board (SERB), Department of Science & Technology, India (No. ECR/2018/001065). Authors express sincere thanks to the support from SERB-DST and SASTRA Deemed University, India.

Author contributions

MD – conceptualization, methodology, investigation, data curation, writing – original draft, VS – characterization, software simulation and validation, writing – original draft, SVM – conceptualization, investigation, funding acquisition, writing – review and editing.

Declarations

Competing interests

The authors declare no competing interests.

Additional information

Correspondence and requests for materials should be addressed to V.M.S.

Reprints and permissions information is available at www.nature.com/reprints.

Publisher's note Springer Nature remains neutral with regard to jurisdictional claims in published maps and institutional affiliations.